scientific reports

Check for updates

OPEN

Decoration of Ag nanoparticles on $CoMoO_4$ rods for efficient electrochemical reduction of CO_2

Schindra Kumar Ray✉, Rabin Dahal, Moses D. Ashie & Bishnu Prasad Bastakoti✉

Hydrothermal and photoreduction/deposition methods were used to fabricate Ag nanoparticles (NPs) decorated $CoMoO_4$ rods. Improvement of charge transfer and transportation of ions by making heterostructure was proved by cyclic voltammetry and electrochemical impedance spectroscopy measurements. Linear sweep voltammetry results revealed a fivefold enhancement of current density by fabricating heterostructure. The lowest Tafel slope (112 mV/dec) for heterostructure compared with $CoMoO_4$ (273 mV/dec) suggested the improvement of electrocatalytic performance. The electrochemical CO_2 reduction reaction was performed on an H-type cell. The $CoMoO_4$ electrocatalyst possessed the Faraday efficiencies (FEs) of CO and CH_4 up to 56.80% and 19.80%, respectively at −1.3 V versus RHE. In addition, Ag NPs decorated $CoMoO_4$ electrocatalyst showed FEs for CO, CH_4, and C_2H_6 were 35.30%, 11.40%, and 44.20%, respectively, at the same potential. It is found that CO_2 reduction products shifted from CO/CH_4 to C_2H_6 when the Ag NPs deposited on the $CoMoO_4$ electrocatalyst. In addition, it demonstrated excellent electrocatalytic stability after a prolonged 25 h amperometric test at −1.3 V versus RHE. It can be attributed to a synergistic effect between the Ag NPs and $CoMoO_4$ rods. This study highlights the cooperation between Ag NPs on $CoMoO_4$ components and provides new insight into the design of heterostructure as an efficient, stable catalyst towards electrocatalytic reduction of CO_2 to CO, CH_4, and C_2H_6 products.

The dramatic increase in CO_2 concentration in the atmosphere leads to notable environmental issues[1]. So, the conversion of CO_2 into valuable chemical products plays a vital role to minimize the greenhouse effect and maintain the global carbon balance that has recently attracted significant attention to researchers[2–6]. Among different CO_2 conversion strategies, the electrochemical CO_2 reduction reaction (CO_2RR) reveals a perfect approach for usable chemicals and fuels productions[7,8]. The combination of carbon-based electro-fuel production from CO_2RR with renewable energy exhibits the great hope of global carbon neutrality. However, slow reaction kinetics lowers the performance of the electrocatalyst for CO_2RR[9,10]. Therefore, fabrication of a novel electrocatalyst is urgent to solve the problems related with sluggish kinetics and high overpotential.

Ag has been regarded as a promising CO_2RR catalyst due to its relatively low overpotential, high selectivity, tendency of lowering the CO_2 reduction reaction barrier, better solubility of CO_2, electron transfer, improvement of local catalytic environment, suppression of hydrogen evolution reaction (HER), and appropriate (neither too strong nor too weak) binding strength with products[11–13]. It is considered as a benchmark electrocatalysts for selective conversion of CO_2 to CO with good Faradic efficiencies. Despite these advantages, pure Ag NPs suffer from maintaining the size/structure, high-cost, and stability due to their high level of surface energy[14]. So, the construction of heterostructure interface between pure metal and low-cost metal oxide materials is a perfect choice because it induces synergistic effects to promote the stability/selectivity/electrocatalytic efficiency, reduce the overpotential, and conversion of CO_2 to CO, C1 and multi-carbon products[10,14].

Nowadays, Ag NPs have been coupled with several metal oxides such as TiO_2, CuOx, Cr_2O_3, MnO_2, SnO_2, etc. for CO_2RR. However, these oxide materials suffer from low conductivity and insufficient catalytic performances[15–19]. Also, these heterostructures cannot produce C2 (C_2H_6) during electrocatalytic CO_2RR. To solve these issues, selecting cobalt molybdate ($CoMoO_4$) is the best metal oxide material because Co-based oxides provide excellent catalytic activities and Mo-based materials demonstrate outstanding electrical conductivity[20]. Also, the synergistic integration of Co and Mo improves the electrocatalytic properties of $CoMoO_4$. In addition, it has several advantages such as stable crystal structure, redox performance, favorable physical/chemical properties, enhancement of electrolyte–electrode surface area, excellent mechanical stability, ionic conductivity, generation of active sites, small overpotential, environmentally friendly, inexpensive, and abundant resources[21–25]. The

Department of Chemistry, North Carolina A and T State University, 1601 E Market St, Greensboro, NC 27411, USA. ✉email: skray@ncat.edu; bpbastakoti@ncat.edu

multiple oxidation states of cobalt involved at the intermediate state for CO_2RR[26]. Furthermore, rods like structure or nanorods can contribute a higher contact area along with great electron pathways than other morphologies[21]. Although lots of paper has been published for Ag NPs towards CO_2RR, Ag NPs decorated $CoMoO_4$ rod heterostructure has rarely been reported for CO_2 reduction to CO, C1 and multi-carbon compounds.

In this study, $Ag/CoMoO_4$ heterostructure was synthesized by hydrothermal and photoreduction/deposition methods. The hydrothermal method revealed several advantages as compared to others, such as low cost, mass efficiency, high product purity, mild preparation conditions, and simple equipment[20,24,27–31]. In addition, photoreduction process is simple and inexpensive and can be operated at room temperature[32]. The formation of heterostructure is well characterized by X-ray diffractometry (XRD), field emission scanning electron microscopy (FESEM), transmission electron microscopy (TEM), elemental mapping, X-ray photoelectron spectroscopy (XPS), Raman spectroscopy, Fourier-transform infrared spectroscopy (FTIR), and Inductively coupled plasma optical emission spectroscopy (ICP-OES). The electrochemical measurements (cyclic voltammetry, electrochemical impedance spectroscopy, linear sweep voltammetry, and chronoamperometry) of catalysts were performed in an H-type cell for electrochemical CO_2RR. Tafel plots were analyzed. The gaseous products were detected by gas chromatography (GC). The Faradic efficiencies (FEs) of CO_2RR was calculated, and possible mechanisms were proposed.

Experimental section

Materials

All chemicals consist of analytical grade. These were used without any further purification. Copper foil (CF) with 0.1 mm thickness was purchased from Merck, Germany. Molybdic acid (H_2MoO_4) and cobalt nitrate hexahydrate [$Co(NO_3)_2.6H_2O$], potassium bicarbonate ($KHCO_3$), and aqueous ammonia (aq. NH_3) were used for the synthesis of samples and obtained from the Sigma-Aldrich. Silver nitrate ($AgNO_3$) was purchased from Fisher chemical, Belgium.

Synthesis of $CoMoO_4$ and $Ag/CoMoO_4$

$CoMoO_4$ was synthesized from hydrothermal process. In this synthesis technique, 2×10^{-2} mol of H_2MoO_4 was placed in 40 mL of water. In addition, 2×10^{-2} mol of $Co(NO_3)_2{\cdot}6H_2O$ was dissolved in 40 mL of water. These were magnetically stirred until clear solution was obtained. Then, the prepared solutions were mixed dropwise by using pipette under magnetic stirring and precipitation was occurred. The pH of the solution was adjusted at pH 7 by using aqueous ammonia (NH_3). It was magnetically stirred for 4 h. After that, the suspension solution was transferred into a 100 mL Teflon-lined stainless autoclave and kept at 200 °C for 4 h. After completion of hydrothermal treatment, the solution was centrifuged and washed with water and ethanol multiple times. Subsequently, it was dried in a vacuum oven at 70 °C for 8 h. The powder was obtained and calcined at 400 °C for 5 h. At last, the powder sample ($CoMoO_4$) was grounded with the help of mortar and piston.

$Ag/CoMoO_4$ was fabricated by hydrothermal followed by photoreduction/deposition techniques. According to this technique, hydrothermal synthesized 1 g of $CoMoO_4$ powder was taken and placed in 100 mL beaker. 80 mL ethyl alcohol (C_2H_5OH) was put in a beaker and magnetically stirred for 2 h. 5 wt% of Ag (source: $AgNO_3$) was placed in a beaker and magnetically stirred for 4 h under UV light irradiation. After this step, it was centrifuged and washed with water/C_2H_5OH several times. The obtained sample was dried in a vacuum oven for 70 °C for 4 h. Finally, it was grounded. The schematic illustration of material synthesis was presented in Fig. S1.

Material characterization

The crystal phase was determined using a powder X-ray diffractometer (Rigaku, Miniflex 600) with Cu Kα radiation (2θ: 20 to 80°, continuous rate: 1°/minute, and step: 0.02). The morphologies of samples were investigated by field emission scanning electron microscopy (FESEM, JEOL, JSM-IT800). Transmission electron microscopy (TEM), high-resolution transmission electron microscopy (HRTEM), and selected area diffraction patterns (SAED), EDS elemental mapping images were obtained by JEOL 1230. The X-ray photoelectron spectroscopy (XPS) analysis of the samples was performed using Thermo Scientific ESCALAB™ XI (Al Kα and 200 eV). The Raman spectra of samples were measured on Horiba Raman confocal microscope. Fourier-transform infrared spectroscopy (FTIR) of samples were measured on IRTracer-100 (Shimadzu). Inductively coupled plasma optical emission spectroscopy (ICP-OES) was used to find the leaching of Ag NPs after performance of electrochemical CO_2 RR by samples. It is also used to find out the metal ions in the samples. The detail explanation was provided in supporting information (Figs. S2, S3, and S4). Zeta potential of powder samples was measured by Zetasizer Nano ZS (Malvern Instruments, Malvern, UK). The powder was dispersed in 70% ethanol (15 mL) and placed in an ultrasonic bath for 1 h. The zeta potential was measured after diluting the samples with distilled water.

Electrochemical characterizations

All the electrochemical measurements were carried out on a CH Instruments with a typical three-electrode system in 0.5 M $KHCO_3$ electrolyte solution at room temperature, a platinum electrode (counter electrode), Ag/AgCl electrode (reference electrode), and working electrodes ($CoMoO_4$ and $Ag/CoMoO_4$). For the synthesis of working electrodes, 0.5 mL of C_2H_5OH, 50 µL nafion, and 4 mg of powder sample were dispersed via ultrasonic processing. As a substrate, CF (2 cm × 2 cm) was washed with water and ethanol for 60 min under ultrasonication and dried at 70 °C for 4 h in a vacuum oven. The well-dispersed ink was placed in CF via controllable drop casting. The available working area in the electrode was 1 cm^2. Then, it was dried in an oven at 70 °C for 4 h.

Cyclic voltammetry (CV) with scan rate 20 to 150 mV/s of samples was measured. In addition, the electrical conductivity of the samples was performed through the electrochemical impedance spectroscopy (EIS)

that consists of 0.1 Hz to 100,000 Hz. The linear sweep voltammetry (LSV) of the samples was observed from 0 to −0.6 V versus RHE at scan rate 10 mV/s. Tafel plots were obtained at potential −1 to 1 V. The reversible hydrogen electrode (RHE) was calculated using following equation: $E_{RHE} = E_{Ag/AgCl} + 0.197 + 0.059$ pH (0.5 M $KHCO_3 \sim 8.52$), where $E_{Ag/AgCl}$ represents potential against the reference electrode and 0.197 V indicates the standard potential of Ag/AgCl at 25 °C[33].

The electrochemical CO_2RR was performed on H-type cell. A 50 mL electrochemical cell was used that consists of 35 mL electrolyte. The anodic and cathodic compartments were separated by Nafion 117 membrane. This membrane was washed with acid/water before using in H-type cell. A stream of pure (99.999%) CO_2 gas was continuously passed in the cell for saturation of electrolyte for 60 min at 5 sccm using mass flow controller (MC-100SCCM-D, Alicat Scientific). The gas outlet of H -type cell (cathodic compartment) was connected to a gas chromatograph (SRI 8610C). The GC is equipped with flame ionization detector (FID) for determining hydrocarbon and CO products during electrochemical CO_2RR. The carrier gas for FID is helium GC was calibrated using standard gas mixtures (ARC3) under 1 atm and 298 K. Amperometry *i-t* experiments were conducted at fixed potentials −1.3 V versus RHE. The first injection of gas in GC was performed 400 s after the start of CO_2 reduction. The different concentration of gases in ppm was noted and Faradic efficiencies were calculated on −1.3 V versus RHE. (Supplementary information). In addition, electrocatalytic stability was evaluated for 25 h under similar applied potential. For comparison of efficiency of electrocatalyst, electrocatalytic performance of the copper foil was carried out.

Results and discussion

Characterization of synthetic materials

As shown in Fig. 1, XRD patterns of samples were well matched with monoclinic structure of pure α-$CoMoO_4$ with space group *C*2/*m* (JCPDS No. 21-0868)[25]. After deposition of Ag NPs on $CoMoO_4$, new crystal plane (111) was appeared that suggests the existence of cubic Ag NPs with JCPDS No. 4-0783[34]. In addition, the intensities of XRD peaks were slightly reduced in Ag/$CoMoO_4$ sample. Besides, it should be noted that the peak position of $CoMoO_4$ was not shifted, which suggested no substitutional doping. No impurities diffraction peaks were found in samples. The existence of Ag and $CoMoO_4$ in Ag/$CoMoO_4$ suggest the successful fabrication of heterostructures.

The morphologies of synthesized materials were investigated by FESEM and TEM. The samples presented rod-like morphology with dimensions of 1–3 µm in length and 0.3–1 µm in width (Fig. 2a and b). The existence of Ag NPs on the $CoMoO_4$ rods was also observed in Fig. 2b. In addition, the loading of Ag NPs on $CoMoO_4$ rods did not change the morphology of materials. Figure 2c and d presented the TEM image of Ag/$CoMoO_4$. This image revealed the decoration of Ag NPs on the surface of $CoMoO_4$ rods. It also indicates the uniform distribution of Ag NPs on rods. The interplanar spacing of 0.33 nm and 0.23 nm calculated from Fig. 2e were corresponds to the (002) and (111) crystal planes of $CoMoO_4$ and Ag, respectively which are also strongest peak in the XRD spectrum. All the interplanar spacing calculated from HRTEM image are well consistent with crystallographic plane of $CoMoO_4$ and Ag. SAED patterns suggested the poly-crystalline nature of Ag/$CoMoO_4$ (Fig. 2f). As shown in Figs. 2g–k and S5, the TEM-EDS mapping/spectrum of Ag/$CoMoO_4$ indicated the existence as well as homogenous distribution of Co, Mo, O, and Ag (Table S1). According to the results of XRD, FESEM, TEM, HRTEM, SAED, and TEM-EDS elemental mapping images, it was concluded that the heterostructure was successfully formed between $CoMoO_4$ and Ag NPs.

The existence of elements and oxidation states in $CoMoO_4$ and Ag/$CoMoO_4$ were investigated using XPS technique (Fig. 3). The Co 2p spectra of samples could be deconvoluted into $2p_{3/2}$, ($CoMoO_4$: 781.12 eV and

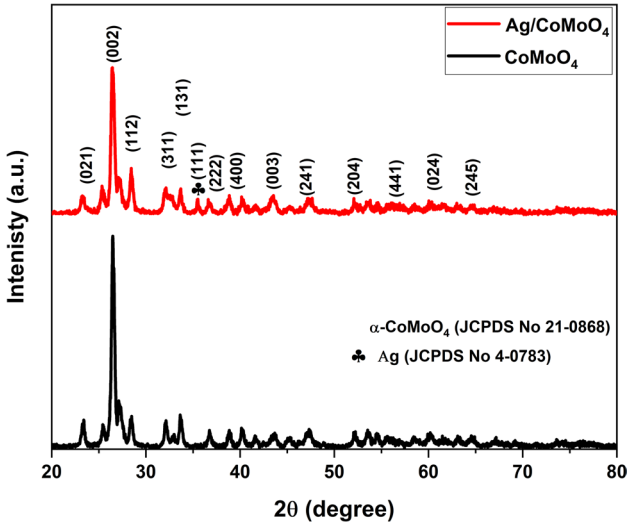

Figure 1. XRD analysis of $CoMoO_4$ and Ag/$CoMoO_4$ samples.

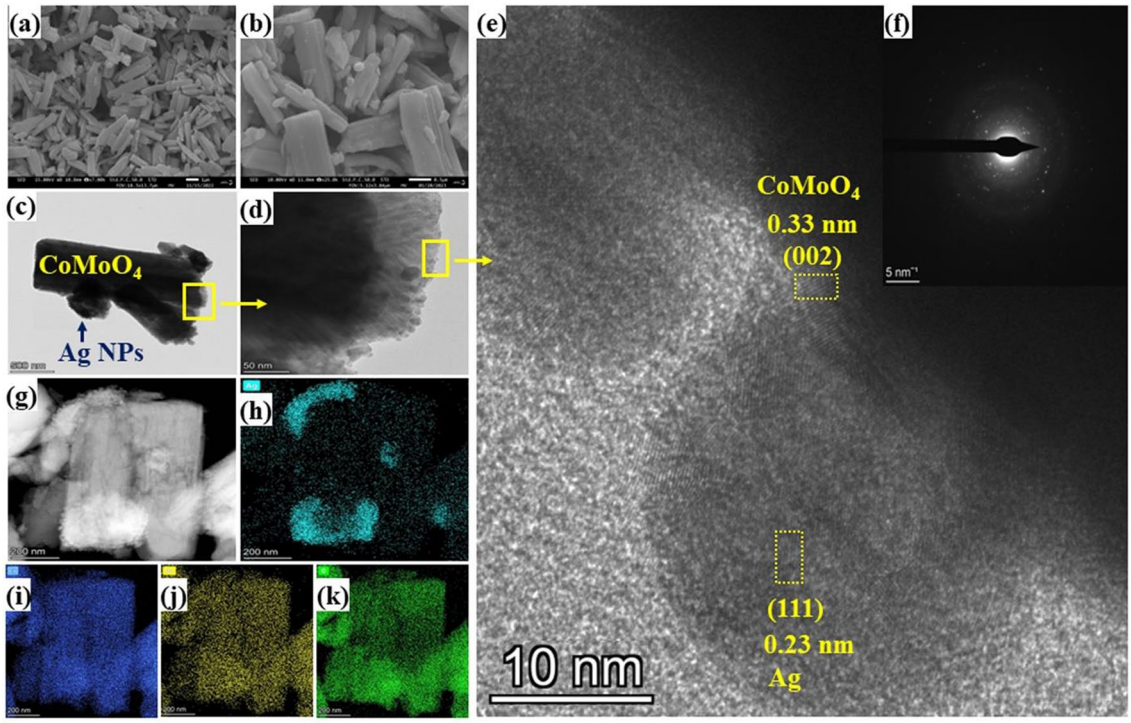

Figure 2. FESEM of (**a**) $CoMoO_4$ and (**b**) $Ag/CoMoO_4$), (**c** and **d**) TEM, (**e**) HRTEM, (**f**) SAED pattern, (**g**–**k**) TEM elemental mapping (**g**: EDS layered image, **h**: Ag, **i**: Co, **j**: Mo, and **k**: O) images of $Ag/CoMoO_4$. Scale bar (**a**: 1 µm, b: 0.5 µm, **c**: 500 nm, **d**: 50 nm, **e**: 10 nm, **f**: 5 nm^{-1}, and **g**–**k**: 200 nm).

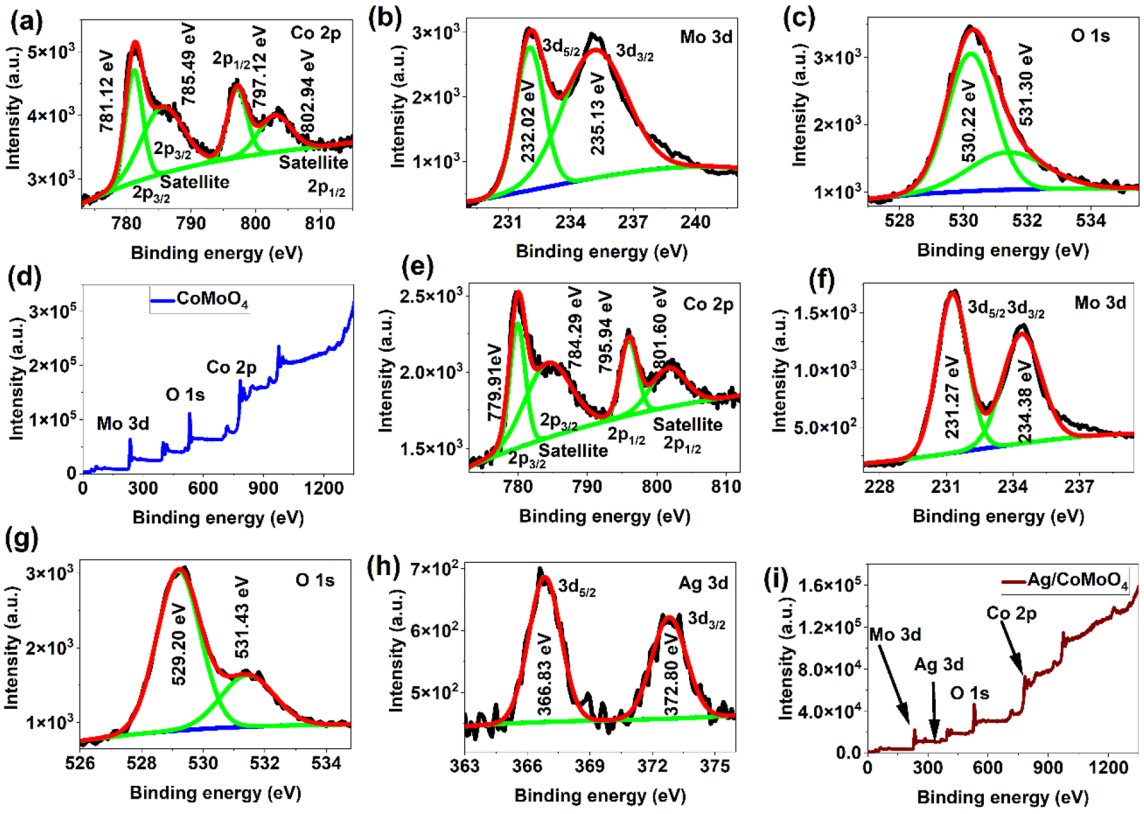

Figure 3. XPS spectra of $CoMoO_4$ (**a**–**d**) and $Ag/CoMoO_4$ (**e**–**i**).

Ag/$CoMoO_4$: 779. 91 eV), satellite $2p_{3/2}$ ($CoMoO_4$: 785.49 eV and Ag/$CoMoO_4$: 784.29 eV), $2p_{1/2}$, ($CoMoO_4$: 797.12 eV and Ag/$CoMoO_4$: 795.94 eV) and satellite $2p_{1/2}$ ($CoMoO_4$: 802.94 eV and Ag/$CoMoO_4$: 801.60 eV) peaks that suggests the Co^{2+} oxidation state in samples (Fig. 3a and e)[35]. The Mo 3d spectra were fitted into two peaks $3d_{5/2}$ ($CoMoO_4$: 232.02 eV and Ag/$CoMoO_4$: 231.27 eV) and $3d_{3/2}$ ($CoMoO_4$: 235.13 eV and Ag/$CoMoO_4$: 234.38 eV). It clearly shows the presence of Mo^{6+} in samples (Fig. 3b and f)[36]. In addition, 0.75 eV and 1.2 eV shift of the binding energy were observed in Mo 3d and Co 2p peaks, respectively. It suggests the evidence for interaction between the $CoMoO_4$ and Ag[37]. According to XPS results of O1s spectra, O^{2-} species in lattice ($CoMoO_4$: 530.22 eV and Ag/$CoMoO_4$: 529.20 eV) and oxygen vacancies ($CoMoO_4$: 531.30 eV and Ag/$CoMoO_4$: 531.30 eV) or defects were observed (Fig. 3c and g)[38]. As shown in Fig. 3h, the presence of metallic Ag NPs in Ag/$CoMoO_4$ was proved by $3d_{5/2}$ and $3d_{3/2}$ peaks at 366.83 eV and 372.80 eV, respectively[39]. Furthermore, the survey spectra suggested the confirmation of Co, Mo, O, and Ag in samples (Fig. 3c and g). Also, the results of ICP-OES indicated the presence of metallic ions (Co, Mo, and Ag) in samples (Supporting information). To find the surface charge in samples, the zeta potential of $CoMoO_4$ and Ag/$CoMoO_4$ was evaluated. The zeta potential of $CoMoO_4$ and Ag/$CoMoO_4$ was -12.30 mV and -15.33 mV, respectively. This results suggests that the surface of both samples are negatively charged.

Raman spectra of $CoMoO_4$ and Ag/$CoMoO_4$ was shown in Fig. S6. The vibrational modes were found at 926, 869, 808.70, and 355.61 cm^{-1}. The Raman mode located at 926.51 cm^{-1} was associated with symmetric stretching mode of doubly coordinated bridging oxygen in Mo–O[40]. The band at 869.20 cm^{-1} was related to the symmetric stretching of Co–O–Mo bond. In addition, the band observed at 808.08 cm^{-1} can be attributed to the asymmetric stretching mode of oxygen in O–Mo–O[41]. The symmetry bending modes of O–Mo–O was observed at 355.61 cm^{-1}[42]. The decoration of Ag NPs on $CoMoO_4$ did not alter the Raman bands that suggest the fabrication of heterojunction between Ag NPs and $CoMoO_4$. Furthermore, FTIR studies were performed of $CoMoO_4$ and Ag/$CoMoO_4$ over the range 500–4000 cm^{-1} (Fig. S7). The band in lower frequency region ($CoMoO_4$: 692.90 cm^{-1} and Ag/$CoMoO_4$: 632.96 cm^{-1}) was associated with Co–Mo–O stretching vibrations[43]. The peaks appeared in $CoMoO_4$ (779.75, 832.78, and 926.54 cm^{-1}) and Ag/$CoMoO_4$ (779.76, 846.01, and 933.40 cm^{-1}) were assigned to Mo–O stretching bands[44]. These bands provided the evidence of $CoMoO_4$ in samples.

Electrochemical CO_2 reduction

As shown in Fig. 4a and b, CV curves of $CoMoO_4$ and Ag/$CoMoO_4$ nanorods were recorded in a potential window of -0.6 to 0.6 V at different sweeping rates (20 mV/s, 40 mV/s, 60 mV/s, 80 mV/s, 100 mV/s, and 150 mV/s). The observed redox peaks may be attributed to reversibly changing their oxidation states of Co^{2+} and Co^{3+}[45]. These redox peaks were obtained from redox mechanism that reveals the Faradic capacitive behavior of the $CoMoO_4$ and Ag/$CoMoO_4$ electrodes. In addition, the enhancement of conductivity by molybdenum (Mo) can improve the electrochemical performances of electrodes[28]. Also, an increase in sweep rate provided the shifting of the oxidation and reduction peaks of electrodes towards right and left, respectively due to higher internal diffusion resistance. The CV curve area and current increased with increase in scan rate because of

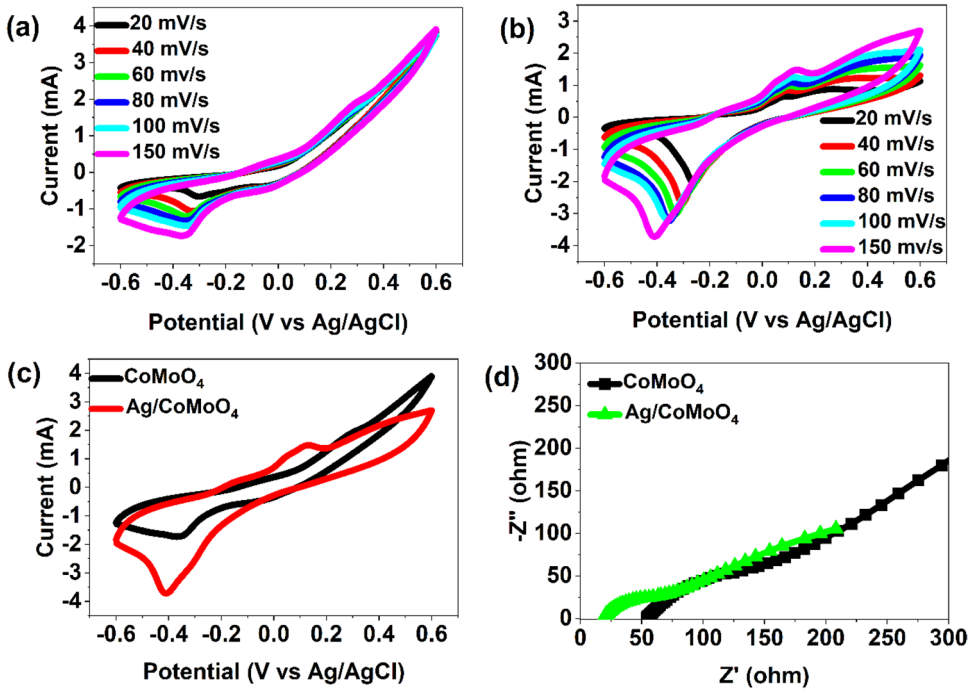

Figure 4. CV (**a**: $CoMoO_4$, (**b**) Ag/$CoMoO_4$, and (**c**) comparison of $CoMoO_4$ and Ag/$CoMoO_4$) and EIS (**d**) of samples.

fast reaction kinetics[27,46]. The shape of CV peaks did not change at high scan rate that suggests the good rate performance of catalyst.

As depicted in Fig. 4c, compared with $CoMoO_4$ electrode, the increased loop of CV curves was observed for $Ag/CoMoO_4$ electrodes. In addition, presence of Ag NPs in $CoMoO_4$ enhanced the reduction ability. These factor indicate the improvement of charge transfer and transportation of ions by making heterostructure between Ag NPs and $CoMoO_4$. So, the fabrication of heterojunction between Ag NPs and $CoMoO_4$ rods enhanced the electrocatalytic performance which is beneficial for CO_2 reduction. To observe the effect of Cu-foil in fabricated electrodes, CV curve of Cu-foil was carried out (Fig. S8). It demonstrates the negligible current as compared to $CoMoO_4$ and $Ag/CoMoO_4$ CV curves. Also, insignificant contribution of Cu-foil was noted. Also, EIS was measured to observe the interfacial charge transfer on catalysts (Fig. 4d)[47]. The obtained data was fitted, and equivalent circuit was made (Fig. S9). It was composed of solution resistance (R1), charge transfer resistance (R2), electric double layer capacitance (C2), Warburg impedance, and constant phase element (Q). According to the Nyquist plots, $Ag/CoMoO_4$ (41.57 Ω) demonstrated lower charge transfer resistance in comparison to $CoMoO_4$ (309.50 Ω) suggesting its rapid electron transfer between the interface of electrolyte and electrocatalyst that may allow efficient electron, Ag NPs and $CoMoO_4$ interactions (Table S2). Therefore, decoration of Ag NPs on $CoMoO_4$ rods could promote the electron transportation between the electrocatalyst and CO_2 molecules that provides the electrochemical reduction capability of heterostructure.

The accelerated CO_2RR conversion kinetics upon the heterostructure was further conformed by Tafel plots (Fig. 5a). The Tafel slope for $CoMoO_4$ and $Ag/CoMoO_4$ were estimated to be 273 mV/dec and 112 mV/dec, respectively. The lowest Tafel slope for $Ag/CoMoO_4$ suggests the enhancement of electrocatalytic activity by fabricating heterostructure between Ag NPs and $CoMoO_4$ because of rapid electron transfer from the electrode to electrocatalyst. This result also indicates that the transfer of first electron to adsorbed CO_2 molecules. It facilitates the production $*CO_2$ that can improve a second electron-transfer for *COOH generation[48]. To compare the electrochemical performance of Ag NPs with other non-precious metal particles, Tafel slope was evaluated (Fig. S10). Ag NPs showed lower Tafel slope than Cu indicating great electrochemical performance of Ag NPs that is accordance to published report[49]. Furthermore, the CO_2RR performance of the as-synthesized electrocatalysts was investigated by LSV graphs (Fig. 5c and d). $Ag/CoMoO_4$ revealed higher current density than $CoMoO_4$ at −0.6 V. Ag NPs decorated $CoMoO_4$ rods showed approximately fivefold enhancement of current density in comparison with $CoMoO_4$ rods (Fig. 5b). The current density of samples along with CO_2-saturated 0.1 M $KHCO_3$ electrolyte suggest demonstrated higher current density suggesting better reactivity in CO_2RR (Fig. 5c).

Steady-state current responses in a CO_2-saturated electrolyte for 400 s at −1.3 V versus RHE of samples were presented in Fig. S11. The obtained current densities for $CoMoO_4$ and $Ag/CoMoO_4$ were −3.35 mA and −4.62 mA, respectively. After that, the gas-phase products were detected by using a GC (Table S3). The FEs for various gas formation of $CoMoO_4$ and $Ag/CoMoO_4$ were calculated (Supporting Information)[33]. According to Fig. 5d, $CoMoO_4$ presented FEs for CO and CH_4 were 56.80% and 19.80%, respectively. In this case, CO and CH_4 act as a major and minor gaseous products during CO_2RR, respectively. In addition, $Ag/CoMoO_4$ revealed FEs for CO and CH_4, and C_2H_6 were 35.30%, 11.40%, and 44.20%, respectively. It was noted that loading of Ag

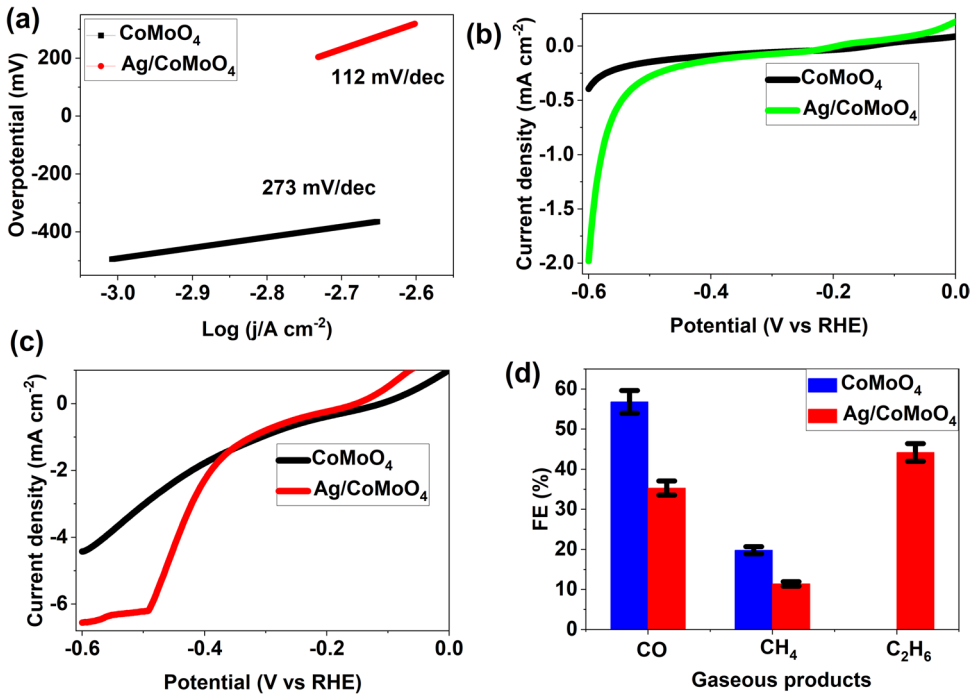

Figure 5. Tafel plots (**a**), LSV (**b**: before CO_2 saturated and **c**: after CO_2 saturated in 0.1 M $KHCO_3$), and FEs (**d**) of samples at −1.3 V versus RHE.

NPs on $CoMoO_4$ reduces the FEs for CO and CH_4, and C_2H_6. These results clearly indicate that C_2H_6 is a major product in Ag NPs decorated $CoMoO_4$ rods. In addition, electrocatalytic stability of cu-foil was evaluated after a 400 s amperometric test at − 1.3 V versus RHE (Fig. S12). Low current density along with unstable nature were observed. It suggests the Cu-foil did not contribute the significantly for steady-state current responses. Stability curves of $Ag/CoMoO_4$ at − 1.3 V versus RHE was shown in Fig. S13. Notably, the electrocatalyst exhibited outstanding stability even upto 25 h. Also, the current density was not changed during stability. ICP-OES analysis of electrolyte solution revealed no leaching of Ag ions after 25 h stability test. Table 1 revealed the comparison of FEs of various Ag-based electrocatalysts with $Ag/CoMoO_4$[16–19,34,48,50,51]. This Table suggests the fabrication of various morphologies of Ag and Ag-based heterostructure by several techniques for electrochemical reduction of CO_2 to CO and C_2H_4 under different applied potential. Although several gaseous products were found on Ag-based electrocatalysts, electrocatalytic reduction of CO_2 into C_2H_6 by using $Ag/CoMoO_4$ heterostructure has not yet been reported in the literature.

Based on the above results, the possible reaction mechanisms/pathways were purposed. In $CoMoO_4$, Co consists of loosely bonded d-electrons that provides the multiple oxidation state. Moreover, transition of Co (II) to Co (I) is considered as an intermediate state for CO_2 reduction[26]. At first, Co^{2+} is reduced to Co^+ under the applied potential. When CO_2 is adsorbed on the (002) catalyst surface, oxidation of Co^+ to Co^{2+} is occurred. Due to this reason, electron is transferred to the adsorbed CO_2 and stabilization of CO_2 radical is happened. Also, the presence of oxygen vacancy in catalyst can improve the stabilization of CO_2 radical[15]. After that, CO_2 radical has ability to capture the proton (H^+) and electron (e^-) that may dissociate from HCO_3^- ion to produce COOH* intermediate because of small potential obstacles. Then, this intermediate reacted with H^+/e^- continuously to generate CO molecule. The possible reasons for formation of CO as a major product is related with existence of π-back donation between the center of Co metal and CO_2 ligand that can enhance the C-O cleavage[52]. Furthermore, *CO may transform into *CHO via hydrogenation[53]. The stabilization of *CHO intermediate play significant role for mitigating the overpotential for CH_4 production. This *CHO intermediate may convert into $*CH_2O$ and $*CH_3O$ during transfer of H^+/e^- during CO_2RR. Finally, $*CH_3O$ intermediate transforms into CH_4[53,54].

The decoration of Ag NPs (111) on the surface of $CoMoO_4$ rod may reduce the energy barrier for conversion of CO_2 to CO, CH_4 and C_2H_6 products that can change the reactions pathways. C–C coupling mechanism plays a vital role to achieve the high selectivity of C_2H_6 species. The possible reason for generation of C_2H_6 species may associate with existence of active sites in catalyst. According to this mechanism, *CO dimerization process is occurred at the catalyst surface[53,55]. The double bond between the C and O is broken and proton can attack the O site to form -OH during reaction with H^+/e^-. In addition, -OH functional group is eliminated with the reaction with proton to produce H_2O. Due to this reaction, double bonds are created between C to C and C to O. After transfer of two H^+/e^-, $2H^+$ react with carbon to form HC=CH along with attachment of O on the surface of catalyst. Then, H^+ may react with double bond containing C to form single bond between carbon along with attachment of O with surface and $-CH_2$. At last, surface attached O reacts with H^+ to form H_2O and C_2H_6 is produced. The possible reason for obtaining the higher FEs of C_2H_6 than CO and CH_4 for $Ag/CoMoO_4$ may associate with higher chance of protonation ($*CO \rightarrow *COH$) than desorption of *CO on interface[56]. Also, decrease in FEs for CO and CH_4 of $Ag/CoMoO_4$ than $COMoO_4$ could be related with covering the Ag NPs on $CoMoO_4$ rods. The synergistic effect between Ag NPs and $CoMoO_4$ rods can be attributed to generate the CO, CH_4 and C_2H_6.

Conclusion

$Ag/CoMoO_4$ electrocatalyst was prepared through hydrothermal and photoreduction/deposition methods. The existence of heterostructure between Ag NPs and $CoMoO_4$ rods was shown by structural and physicochemical characterization techniques. The excellent electrochemical behaviors of catalysts were proved by CV, EIS, LSV, chronoamperometry, and Tafel plots. The electrochemical CO_2RR of $CoMoO_4$ favored for CO (FEs: 56.80) and CH_4 (FEs: 19.80) at − 1.3 V versus RHE in a H-type cell containing 0.5 M $KHCO_3$. However, the heterostructure revealed selectivity for reducing mainly CO_2 to C_2H_6 (FEs: 56.80) along with lower FEs for CO and CH_4 at same condition. The selectivity for reducing CO_2 to CO, CH_4, and C_2H_6 by electrocatalyst was attributed to adequate

Catalyst	Synthesis methods	Morphology	FEs	Potential (V vs. RHE/SCE)	References
Ag-Au	Self-assembly	Nanowires/nanosheet	99.0% (CO)	− 0.9	50
Ag	Chemical/photoreduction	Triangular/nanoplates	96.0% (CO)	− 0.856	51
Ag@ZnO@rGO	Hydrothermal/functionalization	Dodecahedral	70.0% (CO)	− 1.6	34
Ag/CuO	Hydrothermal and impregnation	Nanosphere	40.0% (C_2H_4)	− 1.1	48
Ag/CuO	Solution-phase	Nanosheet	91.2% (CO)	− 0.7	16
Ag/Cr_2O_3	Electrochemical	Hexagon	99.6% (CO)	− 0.8	17
Ag/SnO_2	Oil bath	Sphere	99.2%(CO)	− 0.9	18
Ag/MOx (M = Cr, Sn, Bi, Cu, Pb, and Mn)	Reduction	Dendritic	98.0% (CO)	− 0.7	19
$Ag/CoMoO_4$	Hydrothermal and photoreduction	Rods and nanoparticles	35.30% (CO), 11.40% (CH_4), and 44.20% (C_2H_6)	− 1.3	Our work

Table 1. The comparison of the electrochemical CO_2RR results of this work with other Ag-based electrocatalysts.

active sites, oxygen vacancies, and excellent conductivities. In addition, the synergistic effect of Ag-$CoMoO_4$ active sites provided the C–C coupling for reduction of CO_2 to C_2H_6 electrocatalytically. The electrocatalyst showed excellent stability upto 25 h without reduction of current density that can be applied for practical application towards electrocatalytic CO_2 reduction. The possible mechanisms/pathways were proposed for CO_2RR. Finally, the outcomes of this work present a new approach for improving electrochemical performances/reduction of CO_2 to CO and hydrocarbon by using the Ag/$CoMoO_4$ heterostructure catalyst.

Data availability

The data generated or analysed during this study are available within the article and its supplementary material. Raw data of cyclic voltammetry, Electrochemical Impedance, Faradaic Efficiency, IT curves, LSV plot, Tafel plot, Raman, XPS and XRD spectra are provided in supplementary material (Raw data). All other data is available from the corresponding author upon request.

Received: 2 September 2023; Accepted: 8 January 2024
Published online: 16 January 2024

References

1. Wu, J., Huang, Y., Ye, W. & Li, Y. CO_2 reduction: From the electrochemical to photochemical approach. *Adv. Sci.* **4**, 1–29 (2017).
2. Nitopi, S. *et al.* Progress and perspectives of electrochemical CO_2 reduction on copper in aqueous electrolyte. *Chem. Rev.* **119**, 7610–7672 (2019).
3. Poon, K. C., Wan, W. Y., Su, H. & Sato, H. A review on recent advances in the electrochemical reduction of CO_2 to CO with nano-electrocatalysts. *RSC Adv.* **12**, 22703–22721 (2022).
4. Ejaz, M., Mohamed, M. G. & Kuo, S. W. Solid state chemical transformation provides a fully benzoxazine-linked porous organic polymer displaying enhanced CO_2 capture and supercapacitor performance. *Polym. Chem.* **14**, 2494–2509 (2023).
5. Singh, P. & Srivastava, R. Utilization of bio-inspired catalyst for CO_2 reduction into green fuels: Recent advancement and future perspectives. *J. CO2 Util.* **53**, 101748 (2021).
6. Qin, X., Hansen, H. A., Honkala, K. & Melander, M. M. Cation-induced changes in the inner- and outer-sphere mechanisms of electrocatalytic CO_2 reduction. *Nat. Commun.* **14**, 7607 (2023).
7. Hsu, C. S. *et al.* Activating dynamic atomic-configuration for single-site electrocatalyst in electrochemical CO_2 reduction. *Nat. Commun.* **14**, 1–14 (2023).
8. Sui, R. *et al.* Engineering Ag-Nx single-atom sites on porous concave N-doped carbon for boosting CO_2 electroreduction. *ACS Appl. Mater. Interfaces* **13**, 17736–17744 (2021).
9. Sun, Z., Ma, T., Tao, H., Fan, Q. & Han, B. Fundamentals and challenges of electrochemical CO_2 reduction using two-dimensional materials. *Chem* **3**, 560–587 (2017).
10. Qin, Q., Sun, M., Wu, G. & Dai, L. Emerging of heterostructured materials in CO_2 electroreduction: A perspective. *Carbon Capture Sci. Technol.* **3**, 100043 (2022).
11. Mahyoub, S. A. *et al.* An overview on the recent developments of Ag-based electrodes in the electrochemical reduction of CO_2 to CO. *Sustain. Energy Fuels* **4**, 50–67 (2019).
12. Zhu, D. D., Liu, J. L. & Qiao, S. Z. Recent advances in inorganic heterogeneous electrocatalysts for reduction of carbon dioxide. *Adv. Mater.* **28**, 3423–3452 (2016).
13. Frisch, M. L. *et al.* Unraveling the synergistic effects of Cu-Ag tandem catalysts during electrochemical CO_2 reduction using nanofocused X-ray probes. *Nat. Commun.* **14**, 1–9 (2023).
14. Yang, H. *et al.* Design and synthesis of Ag-based catalysts for electrochemical CO_2 reduction: Advances and perspectives. *Chem. Asian J.* **17**, 1–14 (2022).
15. Ma, S., Lan, Y., Perez, G. M. J., Moniri, S. & Kenis, P. J. A. Silver supported on titania as an active catalyst for electrochemical carbon dioxide reduction. *ChemSusChem* **7**, 866–874 (2014).
16. Zhang, W., Zhu, N., Ding, L., Hu, Y. & Wu, Z. Efficacious CO_2 adsorption and activation on Ag nanoparticles/CuO mesoporous nanosheets heterostructure for CO_2 electroreduction to CO. *Inorg. Chem.* **60**, 19356–19364 (2021).
17. Fu, H. Q. *et al.* Synergistic Cr_2O_3@Ag heterostructure enhanced electrocatalytic CO_2 reduction to CO. *Adv. Mater.* **34**, 2202854 (2022).
18. Li, M., Hu, Y., Wang, D. & Geng, D. Enhanced electrochemical reduction of CO_2 to CO on Ag/SnO_2 by a synergistic effect of morphology and structural defects. *Chem. Asian J.* **16**, 2694–2701 (2021).
19. Yuan, X. *et al.* Interface engineering of silver-based heterostructures for CO_2 reduction reaction. *ACS Appl. Mater. Interfaces* **12**, 56642–56649 (2020).
20. Zhang, Y. *et al.* Structural evolution of $CoMoO_4$ to CoOOH by ion electrochemical etching for boosting oxygen evolution reaction. *J. Power Sources* **442**, 227252 (2019).
21. Alsadat Mohammadi, M., Arvand, M. & Daneshvar, S. Facile stepwise hydrothermal synthesis of hierarchical $CoMoO_4$/$CoMoO_4$ core/shell dandelion-like nanoarrays: A promising binder-free positive electrode for high-performance asymmetric supercapacitors. *J. Electroanal. Chem.* **904**, 115934 (2022).
22. Ray, S. K. & Hur, J. A review on monoclinic metal molybdate photocatalyst for environmental remediation. *J. Ind. Eng. Chem.* **101**, 28–50 (2021).
23. Zhang, L. *et al.* Fabrication of metal molybdate micro/nanomaterials for electrochemical energy storage. *Small* **13**, 1–19 (2017).
24. You, N. *et al.* Constructing P-$CoMoO_4$@NiCoP heterostructure nanoarrays on Ni foam as efficient bifunctional electrocatalysts for overall water splitting. *Nano Mater. Sci.* https://doi.org/10.1016/j.nanoms.2021.05.004 (2021).
25. Jiao, F. *et al.* Regulating the electronic structure of $CoMoO_4$ microrod by phosphorus doping: An efficient electrocatalyst for the hydrogen evolution reaction. *Dalt. Trans.* **49**, 13152–13159 (2020).
26. Usman, M. *et al.* Electrochemical reduction of CO_2: A review of cobalt based catalysts for carbon dioxide conversion to fuels. *Nanomaterials* **11**, 1–27 (2021).
27. Liang, R. *et al.* High performance g-C_3N_4 @$NiMoO_4$/$CoMoO_4$ electrode for supercapacitors. *J. Solid State Chem.* **307**, 122845 (2022).
28. Mao, X. *et al.* Core-shell structured $CuCo_2S_4$@$CoMoO_4$ nanorods for advanced electrode materials. *J. Alloys Compd.* **844**, 156133 (2020).
29. Lakhlifi, H. *et al.* Nanocrystalline transition metal ($CoMoO_4$) prepared by sol gel method: Correlation between powder colors and α/β phase transformations. *Inorg. Chem. Commun.* **145**, 110049 (2022).
30. Adeleye, A. T., John, K. I., Adeleye, P. G., Akande, A. A. & Banjoko, O. O. One-dimensional titanate nanotube materials: Heterogeneous solid catalysts for sustainable synthesis of biofuel precursors/value-added chemicals—a review. *J. Mater. Sci.* **56**, 18391–18416 (2021).

31. Mohan, S., Vellakkat, M., Aravind, A. & Reka, U. Hydrothermal synthesis and characterization of Zinc Oxide nanoparticles of various shapes under different reaction conditions. *Nano Express* **1**, 030028 (2020).
32. Jara, N. *et al.* Photochemical synthesis of gold and silver nanoparticles-a review. *Molecules* **26**, 1–24 (2021).
33. Chen, C. S. *et al.* Stable and selective electrochemical reduction of carbon dioxide to ethylene on copper mesocrystals. *Catal. Sci. Technol.* **5**, 161–168 (2015).
34. Nguyen, V. H. *et al.* Ag@ZnO porous nanoparticle wrapped by rGO for the effective CO_2 electrochemical reduction. *Chem. Eng. Sci.* **232**, 116381 (2021).
35. Wen, Y., Li, C. X., Wang, J., Qian, Y. Y. & Shen, F. C. Hierarchically self-supporting phosphorus-doped $CoMoO_4$ nanoflowers arrays toward efficient hydrogen evolution reaction. *ACS Appl. Energy Mater.* **5**, 6814–6822 (2022).
36. Kumar Ray, S. *et al.* A magnetically separable α-$NiMoO_4$/$ZnFe_2O_4$/coffee biochar heterojunction photocatalyst for efficient ketoprofen degradation. *Chem. Eng. J.* **452**, 139546 (2023).
37. Guo, D. *et al.* Boosting the capacitive performance of hierarchical cobalt molybdate hybrid electrodes for asymmetric supercapacitors. *J. Mater. Sci.* **56**, 10965–10978 (2021).
38. Ray, S. K., Dhakal, D. & Lee, S. W. Insight into malachite green degradation, mechanism and pathways by morphology-tuned α-$NiMoO_4$ photocatalyst. *Photochem. Photobiol.* **94**, 552–563 (2018).
39. Ray, S. K. *et al.* Transformation of tetracycline in water during degradation by visible light driven Ag nanoparticles decorated α-$NiMoO_4$ nanorods: Mechanism and pathways. *Chem. Eng. J.* **373**, 259–274 (2019).
40. de Moura, A. P. *et al.* Photoluminescent properties of $CoMoO_4$ nanorods quickly synthesized and annealed in a domestic microwave oven. *Adv. Chem. Eng. Sci.* **02**, 465–473 (2012).
41. Liu, F. *et al.* Multi-dimensional CuO nanorods supported $CoMoO_4$ nanosheets heterostructure as binder free and high stable electrode for supercapacitor. *J. Mater. Sci. Mater. Electron.* **29**, 10353–10361 (2018).
42. Fang, L. *et al.* Hierarchical $CoMoO_4$ nanoneedle electrodes for advanced supercapacitors and electrocatalytic oxygen evolution. *Electrochim. Acta* **259**, 552–558 (2018).
43. Tantraviwat, D. *et al.* Structural properties of tungsten-doped cobalt molybdate and its application in electrochemical oxygen evolution reaction. *J. Mater. Sci. Mater. Electron.* **29**, 13103–13111 (2018).
44. Harichandran, G., Radha, S., Yesuraj, J. & Muthuraaman, B. Synthesis and characterization of cobalt molybdate dihydrate nanorods arrays for supercapacitor electrode application. *Appl. Phys. A Mater. Sci. Process.* **127**, 1–8 (2021).
45. Gopi, C. V. V. M. *et al.* Facile synthesis of hierarchical flower-like $NiMoO_4$-$CoMoO_4$ nanosheet arrays on nickel foam as an efficient electrode for high rate hybrid supercapacitors. *J. Energy Storage* **30**, 101550 (2020).
46. Elgrishi, N. *et al.* A practical beginner's guide to cyclic voltammetry. *J. Chem. Educ.* **95**, 197–206 (2018).
47. Ray, S. K., Pant, B., Park, M., Hur, J. & Lee, S. W. Cavity-like hierarchical architecture of WS_2/α-$NiMoO_4$ electrodes for supercapacitor application. *Ceram. Int.* **46**, 19022–19027 (2020).
48. Xue, L. *et al.* Ultralow Ag-assisted carbon–carbon coupling mechanism on Cu-based catalysts for electrocatalytic CO_2 reduction. *J. Energy Chem.* **82**, 414–422 (2023).
49. Choi, J. *et al.* Electrochemical CO_2 reduction to CO on dendritic Ag-Cu electrocatalysts prepared by electrodeposition. *Chem. Eng. J.* **299**, 37–44 (2016).
50. Sang, J. L. *et al.* Nanoarchitectonics of 2D-thin and porous Ag-Au nanostructures with controllable alloying degrees toward electrocatalytic CO_2 reduction. *J. Alloys Compd.* **944**, 169155 (2023).
51. Liu, S. *et al.* Shape-dependent electrocatalytic reduction of CO_2 to CO on triangular silver nanoplates. *J. Am. Chem. Soc.* **139**, 2160–2163 (2017).
52. Li, C. *et al.* Carbon dioxide photo/electroreduction with cobalt. *J. Mater. Chem. A* **7**, 16622–16642 (2019).
53. Pei, Y., Zhong, H. & Jin, F. A brief review of electrocatalytic reduction of CO_2—Materials, reaction conditions, and devices. *Energy Sci. Eng.* **9**, 1012–1032 (2021).
54. Xue, L. *et al.* Unveiling the reaction pathway on Cu/CeO_2 catalyst for electrocatalytic CO2 reduction to CH4. *Appl. Catal. B Environ.* **304**, 120951 (2022).
55. Fan, Q. *et al.* Electrochemical CO_2 reduction to C_{2+} species: Heterogeneous electrocatalysts, reaction pathways, and optimization strategies. *Mater. Today Energy* **10**, 280–301 (2018).
56. Shao, B. *et al.* Low-potential-driven electrocatalytic reduction of CO_2 to hydrocarbons by cobalt-based metal-organic nanosheets. *J. Catal.* **413**, 168–175 (2022).

Acknowledgements

This research was supported by National Science Foundation Excellence in Research Award (2100710) USA. The samples were characterized in the Joint School of Nanoscience and Nanoengineering, a member of the Southeastern Nanotechnology Infrastructure Corridor and National Nanotechnology Coordinated Infrastructure, which is supported by the National Science Foundation (Grant ECCS-1542174). The authors would like to express their gratitude to Dr. Kiran Subedi and the Analytical Services Laboratory (ASL) at CAES (College of Agriculture and Environmental Sciences) for their assistance with elemental analysis.

Author contributions

S.K.R. did experiment and wrote manuscript. R.D. and M.D.A. contribute in materials characterization and revision of the manuscript. B.P.B. supervised the project and revised the manuscript. All authors reviewed the manuscript.

Competing interests

The authors declare no competing interests.

Additional information

Supplementary Information The online version contains supplementary material available at https://doi.org/10.1038/s41598-024-51680-w.

Correspondence and requests for materials should be addressed to S.K.R. or B.P.B.